



Universiteit
Leiden
The Netherlands

Hysterons and pathways in mechanical metamaterials

Ding, J.

Citation

Ding, J. (2023, May 31). *Hysterons and pathways in mechanical metamaterials*. *Casimir PhD Series*. Retrieved from <https://hdl.handle.net/1887/3619565>

Version: Publisher's Version

License: [Licence agreement concerning inclusion of doctoral thesis in the Institutional Repository of the University of Leiden](#)

Downloaded from: <https://hdl.handle.net/1887/3619565>

Note: To cite this publication please use the final published version (if applicable).

APPENDIX

In this appendix, we describe techniques for sample fabrication, experimental protocols, and numerical details used in this thesis.

A.1 Molding

In this appendix, we demonstrate the detail of molding of the sample. We make the sketch of the mold by Autodesk Inventor, and save it as an ".stl" file. Then we use Cura to set the printing details. The mold is designed to be broken easily so that we can get the rubber out of the mold without damaging the rubber. Therefore, the thickness of the wall and the base of the mold is 0.2 - 0.6 mm. We design the wall line account of the hollow cylinder 2 mm and the thickness of the hollow cylinder 1.2 mm to make sure that the upper PLA has been printed before the substrate PLAs cool down and the hollow cylinder is stable enough after the printing completed. We also design the thickness of the bottom of every hollow cylinder as 0.8 mm to make sure the hollow cylinder that sticks to the base firmly. The height of each printed layer of the mold is set to be 0.1 mm. The print speed is set to be 50 mm per sec. Then we save both the design and the setting of printing as a ".gcode" file and use the Ultimaker 2+ to print it out.

To making a rubber sample, we first use a spoon and a beaker to mix the two two component elastomers together. The mixture was stirred for 30

to 60 seconds at room temperature and then poured into the mold. The height of the liquid surface is the same as the height of the cylinder of the mold, so that the holes of the sample will not be sealed by a layer of rubber. We use a knife to clean most of the excess rubber.

Next, we eliminate the bubbles in the mixture by putting the mold into a freezer. There are a lot of bubbles that appear in the mixture due to the stirring, and it is necessary to eliminate the influence of bubbles [2, 3]. It takes a long time for the bubbles to rise and disappear in the mixture but it only takes 20 minutes at room temperature for the mixture to almost solidify into rubber. We can reduce the number of bubbles in the sample by speeding up the rise of the bubbles or by prolonging the time the mixture solidifies. The method used in this thesis is extending the solidification time of the rubber. We put the mold into a freezer at -18°C for 1 hour to slow down cross linking, leaving time for the material to degas and fill every nook and cranny in the mold,

After the liquid rubber has solidified, we remove the sample from the mold (Fig. A.1a). After the sample rests for an hour at room temperature, we break the mold to take the sample out of the mold. It is possible for a layer of rubber to cover the cylinder, as shown in Fig. A.1 (b). This thin layer of rubber will seal the hole. To avoid that, we use a knife to remove this layer first. Then we use a knife to cut the base of the mold, as shown in the lower part of Fig. A.1 (c), and after that we use a screw driver or a stick to separate the cylinders from the sample (upper part of the Fig. A.1c). Hence, we can see the result of cutting clearly. The last step to get the sample is pushing out the cylinders by a hexagon screwdriver and removing the walls. Now the final sample is shown in Fig. A.1 (d). We let the sample rest for a week at room temperature, after which the elastomer does not age anymore [2, 3].

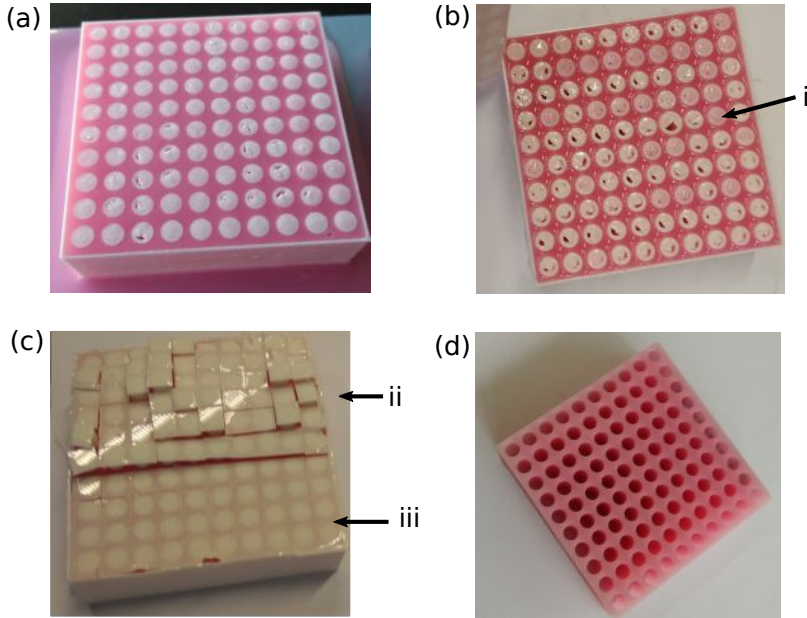


FIGURE A.1: The process of sample manufacture. (a) A mold with solid rubber in it. (b) An example of the cylinder of the mold covered by a little rubber, as (i) shows. (c) The base of the mold was cut by a knife, where (i) is the cut part being separated and (ii) is the cut part not being separated. (d) A sample.

A.2 Sample Preparation

A.2.1 3D Printing of molds

We create flexible metamaterials by pour two component elastomers into 3D printed molds. We use an Ultimaker to print the mold with 2.85 mm Filament Performa PLA(Polylactic Acid), and the diameter of the nozzle of the printer is 0.4 mm. We first describe the mold used for a square sample with 4 straight borders, followed by a description of the mold used to fabricate samples without borders in two opposite sides.

We first focus on the creation of square samples (10×10 holes) with 4 straight borders. A typical mold is shown in Fig. A.2. It is designed to make a $H \times W \times T = 50 \text{ mm} \times 50 \text{ mm} \times 15 \text{ mm}$ sample. The mold was designed by Autodesk Inventor. The mold is created like a container to pour the liquid elastomer components without leaking, and there are cylinders in the mold to make the holes in the sample. The outer length of the square mold is 51 mm, and the outer height of the mold is 15 mm.

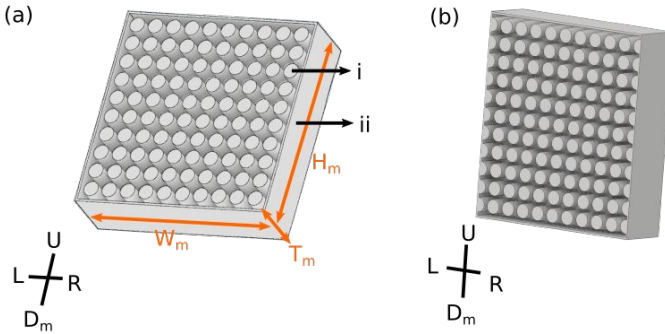


FIGURE A.2: The mold of the 10×10 biholey metamaterial. We call the sides with walls upper(U) and down (D_m) side while the sides without walls are the left(L) and right(R) sides. (a) A mold of a sample with sidewalls, which includes: (i) the cylinder in the mold and (ii) the side walls. The pitch between two cylinders, P , is 5 mm; the diameter of the cylinder, D , is 4 mm; the spacing between 2 cylinders is 1 mm; the spacing between a cylinder and the wall is 1 mm; the thickness of the wall is 0.5 mm, $W_m = H_m = 51.0 \text{ mm}$, and $T_m = 15.5 \text{ mm}$. (b) A mold of a sample without sidewalls, which dimension is $51 \text{ mm} \times 57 \text{ mm} \times 15.3 \text{ mm}$.

Another type of mold of the sample without side walls is created like a container with 11×9 holes inside the container and 11×2 half holes connecting the wall to the mold. The cylinders inside are to make the holes on the holey sheet while the half cylinders connecting the wall of the mold are to make the side wall flexible [2, 3]. A typical mold is shown in Fig. A.2. It is designed to make a $50 \text{ mm} \times 56 \text{ mm} \times 15 \text{ mm}$ sample with 11×9 holes and 11×2 half holes. For the setting of printing and designing of the mold without side walls at the left and right of the sample, we use the same design as above (for details see appendix).

Once we have printed the mold, we can pour silicon rubber into the mold. The rubber we used for the sample is two component silicon elastomer, brand name *Elite Double 8* from Zhermack, with a Young's Modulus $E \approx 220kPa$, Poisson's ratio $\nu \approx 0.5$, The two components are the polymer and the catalyst respectively and the two components should be mixed at 1:1 weight ratio. For detail, see appendix.

A.2.2 Geometric error bar

No.	D_d (mm)	D (mm)	Error Bars of D (mm)	D_i (mm)	Error Bars of D_i (mm)
1	3.50	3.40	0.05	3.35	0.19
2	4.00	3.90	0.05	3.80	0.30
3	4.50	4.40	0.10	4.35	0.26
4	4.50	4.50	0.05	4.50	0.33

TABLE A.1: Parameters of the holes in the homogeneous holey samples with side walls. The sample (10×10) is characterized with $\{H, W, T, P\} = \{51 \text{ mm}, 51 \text{ mm}, 15 \text{ mm}, 5 \text{ mm}\}$.

Now we discuss the geometric differences and Root Mean Square (RMS) errors in the sample, and focus on the mean and errorbar of the diameter of the holes in a sample. We compare the originally designed diameter, D_d , the diameter of the cylinder of the printed mold, D , and the diameter measured in a snapshot of the rubber sample, D_i . Among them, D_d is affected by printer accuracy, D_i is affected by rubber aging, and D is measured in a snapshot of the sample through image J. Tab. A.1 shows the diameters and RMS error bars of the printed samples. In this thesis, we use the diameter of the cylinder of the printed mold D as the geometry of hole pattern.

A.3 Experimental Protocol

A.3.1 Uniaxial Testing

We probe the samples by a dual column Instron 5965 uniaxial compression device. The sample is put on the Instron between the ground plate and the compression plate, as shown in Fig. A.3 (a).

The Instron moves the horizontal cross bar in vertical direction to compress or decompress the sample. The resolution of the vertical displacement of the horizontal cross bar is $4\ \mu\text{m}$. The resulting force is measured with a 100 N load cell attached to the horizontal bar and the resolution of the load cell is 0.5 mN. We use a computer to control the Instron using BlueHill 2 to preset the displacement and the speed of the horizontal bar. During the testing, two constant nominal compression rates, $\pm 0.2\ \text{mm/sec}$, applied on the sample. At last, the force data of the response collected by the load cell and saved as a '.csv' file.

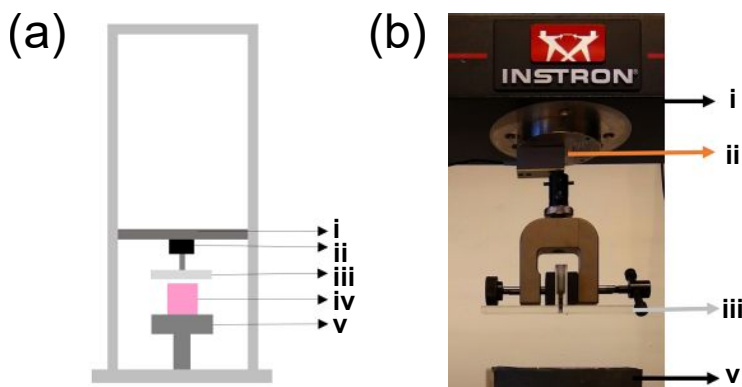


FIGURE A.3: (a) The sketch of the Instron, where (i) denotes the horizontal cross bar, (ii) denotes load cell of the force sensor, (iii) denotes the compression plate, (iv) denotes the sample, and (v) denotes the support plate. (b) A photo of the Instron.

A.3.2 Image acquisition

The camera we used to acquire images is a Basler asA2040-25gm/gc CMOS camera. It is 2046×2046 pixels and the size of each pixel is $5.5 \times 5.5 \mu\text{m}$. Fig. A.4 shows the schematic diagram of the setup of the camera. There are two possible setups for the light. Fig. A.4 (a) shows the setup of the sample illuminated by light in front of it, while Fig. A.4 (b) shows the setup of the outline of the sample illuminated by a back light. The camera is placed approximately 90 cm away of the sample to minimize distortion and parallax. Then we focus and magnify the sample to show it in the center of the camera. The camera is connected to the same computer as the Instron testing device and is controlled by LabView, so we can acquire image while measuring force and displacement data with the Instron. When we start testing by the BlueHill 2 in the computer, the horizontal bar start moving vertically, the load cell start recording data and the camera start taking image. The exposure time of the camera is between 150 ms and 750 ms. Hence we can get 400 to 80 images per minutes. Photos are saved as '.png' files automatically and the precise times of taking each photo are saved as '.txt' file.

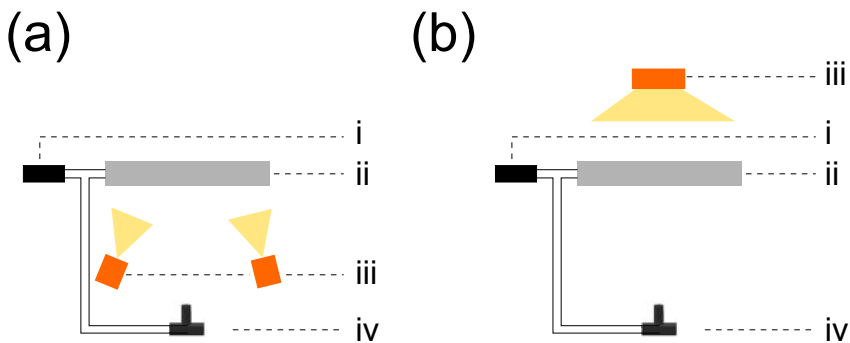


FIGURE A.4: Overview of the setup of the camera, where (i) denotes the computer, (ii) denotes Instron, (iii) denotes the light, and (iv) denotes the camera. (a) Front light setup. (b) Backlight setup.

A.3.3 Experimental details

We start the experiment by placing the sample in the Instron. Then we adjust the camera. Firstly, we turn on the LED light and keep it on during the experiment. Secondly, we observe the view of the camera by starting the LabView NI-DAQmx Measurement & Automation Explorer software to control the camera, turning off the trigger mode box, and playing the 'capture images continuously'. We adjudge the position to make the sample in the center of the view of the camera. Now we adjust the lens of the camera so that the entire sample can fill the image taken by the camera. If needed, we also adjudge the position of the sample and the aperture of the camera. After that, we turn on the the trigger mode box of LabView NI-DAQmx Measurement & Automation Explorer to make sure the Bluehill 2 can trigger the camera.

Next, we start the Bluehill 2 software. We lower the crossbar until the T-shaped compression plate is 1 or 2 mm away from the sample so that we can track the entire process from when the compression plate has not touched the sample to the compression plate compressing the sample. Now we reset the height of the crossbar and the force, using 'Reset Gauge' button and 'Balance Load' button.

Next, we design a test that allows us to compress and decompress the sample by an amount u_y with a rate of v_y and save the data in a .csv file, where the columns are Time, Compression Strain (raw strain) and Compression Stress (raw stress). We use a compression rate at 0.2 mm/sec.

Next, we trigger both Instron and the camera to start the experiment. In parallel, we start our self-written LabView program[2, 3] that captures the photos taken by the camera which is triggered by the SYNC pulse. Then, we start the Bluehill program immediately after LabView Program such that we can collect images and the compression data.

The image and the compression data are all saved in a folder named by the date. Under this folder, the images are saved in a subfolder called 'photo' and the raw data saved in a subfolder called 'XXX.is_comp_RawData' or 'XXX.is_ccyclic_RawData', where XXX is the name of the sample.

A.4 FEM analysis and the type of element

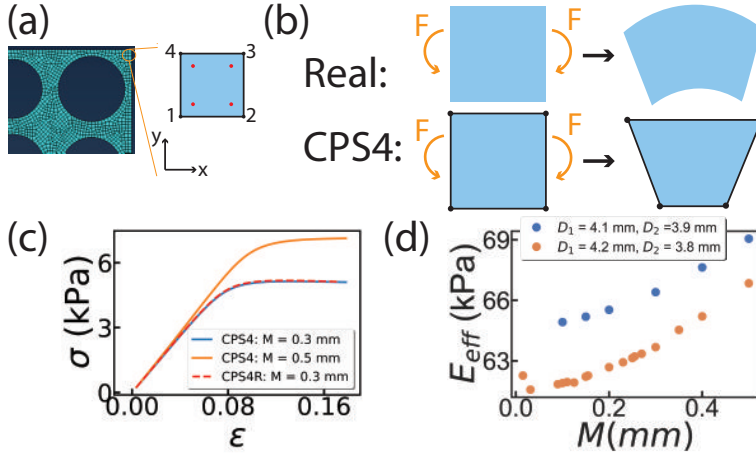


FIGURE A.5: The 2D bihole metamaterial with 5 by 5 holes is meshed with CPS4. (a) An example of CPS4. The red dot is the integration point for output. The black dot and line are the ordered node and face on the element respectively. (b) An example of the real element bending and an example of the actual shape of a corresponding CPS4 element. The orange curves denote the force on the element. (c) The resulting $\epsilon - \sigma$ curve ($P = 5$ mm, $D_1 = 4.1$ mm, $D_2 = 3.9$ mm). (d) The resulting $M - E_{eff}$ plot of the sample with element type - CPS4.

We use the finite element package Abaqus/Standard [2, 3, 11, 19, 25] to obtain the first mode of the bihole metamaterial, which provide a 'static', uniaxial, vertical compression on the sample. To do the finite element analysis, we divide the domain of the problem into a collection of subdomains: this is called meshing. The biggest size of the mesh is $t/3$, where t is the thickness of the filament between two holes. To investigate the influence of the choice of the mesh, we compare two different element types and apply

the elements on the 2D biholey sheet with 5 by 5 holes sample, as shown in Fig. A.5 (a) and Fig. A.6 (a).

One type of element we use is a 4-node bilinear plane strain quadrilateral (CPS4), as shown in Fig. A.5 (a). Fig. A.5 (b) shows an example of a deformed CPS4, which illustrate that deformation of this element are trapezoidal. CPS4 elements have 4 straight sides because each side uses linear interpolation for position and displacement. As a result, there is a difference between the simulations and reality, so that the simulation results may depend on the density of the nodes, which is also known as mesh size, M .

To study the effect of meshing on the deformation, we have performed a systematic mesh refinement study for the in-plane grid and varied the mesh size. Fig. A.5 (c) shows the force response of a biholey metamaterial with 5 by 5 holes ($P = 5$ mm, $D_1 = 4.1$ mm, $D_2 = 3.9$ mm) and meshed in different sizes. With regard to the element type CPS4, we see the smaller mesh size ($M = 0.3$ mm) provides a softer response. Fig. A.5 (d) shows that the effective Young's Modulus, E_{eff} , of two biholey metamaterials with different geometry changes with M , where E_{eff} is the slope of the liner increasing part of the $\varepsilon - \sigma$ curve. We see E_{eff} increases with M . We note that the value of the sample with $D_1 = 4.1$ mm, $D_2 = 3.9$ mm and $M = 0.4$ mm have a larger value than the sample with $D_1 = 4.2$ mm, $D_2 = 3.8$ mm and $M = 0.1$ mm, which means M has a significant effect on the force response of the sample.

Sometimes, we also reduce integration with hourglass control in CPS4 (CPS4R), which only outputs one integration point and provides a faster calculation speed, but the simulation result of the element type CPS4R is close to CPS4. In Fig. A.5 (c), there is an example of the simulation result of the element type CPS4R, and we see the red dash line almost coincident with the blue line.

We also studied the eight-node plane stress element, CPS8, as shown in Fig. A.6 (a). Since each side of the CPS8 has 3 nodes, it is able to use

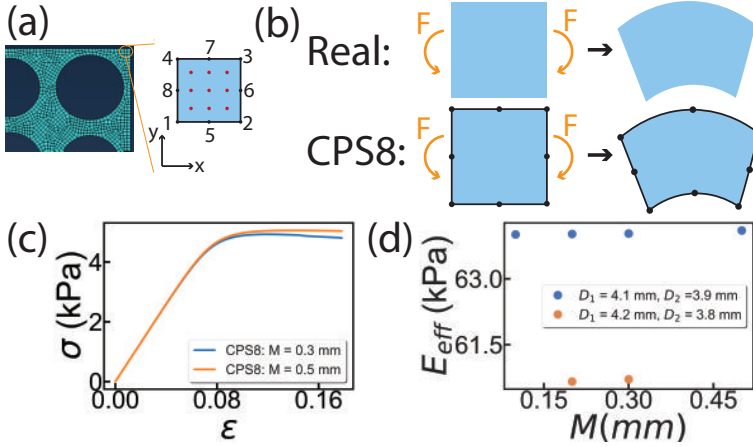


FIGURE A.6: The 2D bihole metamaterial with 5 by 5 holes is meshed with CPS8. (a) An example of CPS8. The red dot is the integration point for output. The black dot and line are the ordered node and face on the element respectively. (b) An example of the real element bending and an example of the actual shape of a corresponding CPS8. The orange curves denote the force on the element. (c) The resulting $\epsilon - \sigma$ curve ($P = 5$ mm, $D_1 = 4.1$ mm, $D_2 = 3.9$ mm). The curve of the sample with CPS4: $M = 0.3$ mm and the curve of the sample with CPS4R: $M = 0.3$ mm overlap. (d) The resulting $M - E_{eff}$ plot of the sample with element type - CPS8.

quadratic interpolation for position and displacement so that the strain varies linearly along with the element. Fig. A.6 (b) shows an example of the compression of the deformations of a real element and a CPS8. We see the simulation result of deformation of CPS8 is closed to the real case. Fig. A.6 (c) shows the force response of the bihole metamaterial with 5 by 5 holes ($P = 5$ mm, $D_1 = 4.1$ mm, $D_2 = 3.9$ mm) and meshed in different sizes, and we see the two $\sigma - \epsilon$ curve are close to each other. Fig. A.6 (d) shows more simulation result of the E_{eff} of two bihole metamaterial with different geometry. We see for the two kinds of geometric (blue plots and orange plots), E_{eff} is little affected by M .

Even though the simulation result of elements with type CPS4 is larger than type CPS8, CPS4 is available in both static and dynamic problems. Hence in Chapter 2, we use the element CPS4R to solve the dynamic problem with

a faster calculation speed than CPS4. However, in Chapter 5, to get the first mode of the holey metamaterial, we only consider the static case, so in the following sections, we will use CPS8 in the simulation.

BIBLIOGRAPHY

- [1] K. Bertoldi, V. Vitelli, J. Christensen, and M. Van Hecke, "Flexible mechanical metamaterials," *Nat. Rev. Mater.*, vol. 2, no. 11, pp. 1–11, 2017.
- [2] B. Florijn, C. Coulais, and M. van Hecke, "Programmable mechanical metamaterials," *Phys. Rev. Lett.*, vol. 113, no. 17, p. 175503, 2014.
- [3] B. Florijn, C. Coulais, and M. van Hecke, "Programmable mechanical metamaterials: the role of geometry," *Soft Matter*, vol. 12, no. 42, pp. 8736–8743, 2016.
- [4] C. Coulais, A. Sabbadini, F. Vink, and M. van Hecke, "Multi-step self-guided pathways for shape-changing metamaterials," *Nature*, vol. 561, no. 7724, pp. 512–515, 2018.
- [5] C. Coulais, E. Teomy, K. De Reus, Y. Shokef, and M. Van Hecke, "Combinatorial design of textured mechanical metamaterials," *Nature*, vol. 535, no. 7613, pp. 529–532, 2016.
- [6] A. S. Meeussen, E. C. Oğuz, Y. Shokef, and M. v. Hecke, "Topological defects produce exotic mechanics in complex metamaterials," *Nat. Phys.*, vol. 16, no. 3, pp. 307–311, 2020.
- [7] C. Findeisen, J. Hohe, M. Kadic, and P. Gumbsch, "Characteristics of mechanical metamaterials based on buckling elements," *J. Mech. Phys. Solids*, vol. 102, pp. 151–164, 2017.
- [8] R. Lakes, *Advances in negative Poisson's ratio materials*, vol. 5. Wiley Online Library, 1993.

BIBLIOGRAPHY

- [9] J. N. Grima, R. Gatt, N. Ravirala, A. Alderson, and K. E. Evans, "Negative poisson's ratios in cellular foam materials," *Materials Science and Engineering: A*, vol. 423, no. 1-2, SI, pp. 214–218, 2006.
- [10] G. W. Milton and A. V. Cherkaev, "Which elasticity tensors are realizable?," *J. Eng. Mater. Technol.*, vol. 117, no. 4, p. 483 – 493, 1995.
- [11] K. Bertoldi, P. M. Reis, S. Willshaw, and T. Mullin, "Negative poisson's ratio behavior induced by an elastic instability," *Adv. Mater.*, vol. 22, no. 3, pp. 361–366, 2010.
- [12] J. L. Silverberg, A. A. Evans, L. McLeod, R. C. Hayward, T. Hull, C. D. Santangelo, and I. Cohen, "Using origami design principles to fold reprogrammable mechanical metamaterials," *Science*, vol. 345, no. 6197, pp. 647–650, 2014.
- [13] P. Dieleman, N. Vasmel, S. Waitukaitis, and M. van Hecke, "Jigsaw puzzle design of pluripotent origami," *Nature Physics*, vol. 16, no. 1, pp. 63–68, 2020.
- [14] A. Bossart, D. M. Dykstra, J. Van der Laan, and C. Coulais, "Oligo-modal metamaterials with multifunctional mechanics," *Proc. Natl. Acad. Sci. U. S. A.*, vol. 118, no. 21, p. e2018610118, 2021.
- [15] L. C. van Laake, J. de Vries, S. M. Kani, and J. T. Overvelde, "A fluidic relaxation oscillator for reprogrammable sequential actuation in soft robots," *Matter*, vol. 5, no. 9, pp. 2898–2917, 2022.
- [16] A. Rafsanjani, A. Akbarzadeh, and D. Pasini, "Snapping mechanical metamaterials under tension," *Adv. Mater.*, vol. 27, no. 39, pp. 5931–5935, 2015.
- [17] M. Mungan, S. Sastry, K. Dahmen, and I. Regev, "Networks and hierarchies: How amorphous materials learn to remember," *Phys. Rev. Lett.*, vol. 123, no. 17, p. 178002, 2019.
- [18] H. Bense and M. van Hecke, "Complex pathways and memory in compressed corrugated sheets," *Proc. Natl. Acad. Sci. U. S. A.*, vol. 118, no. 50, p. e2111436118, 2021.

- [19] Z. Zhang, S. Pusateri, B. Xie, and N. Hu, "Tunable energy trapping through contact-induced snap-through buckling in strips with programmable imperfections," *Extreme Mech. Lett.*, vol. 37, p. 100732, 2020.
- [20] D. Melancon, A. E. Forte, L. M. Kamp, B. Gorissen, and K. Bertoldi, "Inflatable origami: Multimodal deformation via multistability," *Adv. Funct. Mater.*, vol. 32, no. 35, p. 2201891, 2022.
- [21] N. C. Keim, J. D. Paulsen, Z. Zeravcic, S. Sastry, and S. R. Nagel, "Memory formation in matter," *Rev. Mod. Phys.*, vol. 91, no. 3, p. 035002, 2019.
- [22] S. An, B. Kim, S. Kwon, G. Moon, M. Lee, and W. Jhe, "Bifurcation-enhanced ultrahigh sensitivity of a buckled cantilever," *Proceedings of the National Academy of Sciences*, vol. 115, no. 12, pp. 2884–2889, 2018.
- [23] Z. Bažant and L. Cedolin, *Stability of Structures: Elastic, Inelastic, Fracture and Damage Theories*. Oxford, U.K.: Oxford University Press, 1991.
- [24] D. Restrepo, N. D. Mankame, and P. D. Zavattieri, "Phase transforming cellular materials," *Extreme Mech. Lett.*, vol. 4, pp. 52–60, 2015.
- [25] J. Liu, H. Qin, and Y. Liu, "Dynamic behaviors of phase transforming cellular structures," *Compos. Struct.*, vol. 184, pp. 536–544, 2018.
- [26] B. Gorissen, D. Melancon, N. Vasios, M. Torbati, and K. Bertoldi, "Inflatable soft jumper inspired by shell snapping," *Science Robotics*, vol. 5, no. 42, p. eabb1967, 2020.
- [27] H. Yang and L. Ma, "Multi-stable mechanical metamaterials by elastic buckling instability," *J. Mater. Sci.*, vol. 54, no. 4, pp. 3509–3526, 2019.
- [28] S. Sun, N. An, G. Wang, M. Li, and J. Zhou, "Snap-back induced hysteresis in an elastic mechanical metamaterial under tension," *Appl. Phys. Lett.*, vol. 115, no. 9, p. 091901, 2019.
- [29] Y. Zhang, M. Tichem, and F. van Keulen, "Rotational snap-through behavior of multi-stable beam-type metastructures," *Int. J. Mech. Sci.*, vol. 193, p. 106172, 2021.

BIBLIOGRAPHY

- [30] Y. Zhang, Y. Wang, and C. Chen, "Ordered deformation localization in cellular mechanical metamaterials," *J. Mech. Phys. Solids*, vol. 123, pp. 28–40, 2019.
- [31] E. Medina, P. E. Farrell, K. Bertoldi, and C. H. Rycroft, "Navigating the landscape of nonlinear mechanical metamaterials for advanced programmability," *Phys. Rev. B.*, vol. 101, no. 6, p. 064101, 2020.
- [32] S. H. Kang, S. Shan, W. L. Noorduin, M. Khan, J. Aizenberg, and K. Bertoldi, "Buckling-induced reversible symmetry breaking and amplification of chirality using supported cellular structures," *Adv. Mater.*, vol. 25, no. 24, pp. 3380–3385, 2013.
- [33] S. Shan, S. H. Kang, J. R. Raney, P. Wang, L. Fang, F. Candido, J. A. Lewis, and K. Bertoldi, "Multistable architected materials for trapping elastic strain energy," *Adv. Mater.*, vol. 27, no. 29, pp. 4296–4301, 2015.
- [34] T. Mullin, S. Deschanel, K. Bertoldi, and M. C. Boyce, "Pattern transformation triggered by deformation," *Phys. Rev. Lett.*, vol. 99, no. 8, p. 084301, 2007.
- [35] K. Bertoldi, M. C. Boyce, S. Deschanel, S. Prange, and T. Mullin, "Mechanics of deformation-triggered pattern transformations and superelastic behavior in periodic elastomeric structures," *J. Mech. Phys. Solids*, vol. 56, no. 8, pp. 2642–2668, 2008.
- [36] C. G. Johnson, U. Jain, A. L. Hazel, D. Pihler-Puzović, and T. Mullin, "On the buckling of an elastic holey column," *Proc. R. Soc. A*, vol. 473, no. 2207, p. 20170477, 2017.
- [37] J. T. Overvelde and K. Bertoldi, "Relating pore shape to the nonlinear response of periodic elastomeric structures," *J. Mech. Phys. Solids*, vol. 64, pp. 351–366, 2014.
- [38] D. Yang, L. Jin, R. V. Martinez, K. Bertoldi, G. M. Whitesides, and Z. Suo, "Phase-transforming and switchable metamaterials," *Extreme Mech. Lett.*, vol. 6, pp. 1–9, 2016.
- [39] Y. Zhang, B. Li, Q. Zheng, G. M. Genin, and C. Chen, "Programmable and robust static topological solitons in mechanical metamaterials," *Nat. Commun.*, vol. 10, no. 1, pp. 1–8, 2019.

- [40] D. Shohat, D. Hexner, and Y. Lahini, "Memory from coupled instabilities in unfolded crumpled sheets," *Proceedings of the National Academy of Sciences*, vol. 119, no. 28, p. e2200028119, 2022.
- [41] L.-Y. Zhang, X. Yin, J. Yang, A. Li, and G.-K. Xu, "Multilevel structural defects-induced elastic wave tunability and localization of a tensegrity metamaterial," *Compos. Sci. Technol.*, vol. 207, p. 108740, 2021.
- [42] H. Yang and L. Ma, "1d to 3d multi-stable architected materials with zero poisson's ratio and controllable thermal expansion," *Mater. Des.*, vol. 188, p. 108430, 2020.
- [43] S. Waitukaitis, R. Menaut, B. G.-g. Chen, and M. Van Hecke, "Origami multistability: From single vertices to metasheets," *Phys. Rev. Lett.*, vol. 114, no. 5, p. 055503, 2015.
- [44] M. van Hecke, "Profusion of transition pathways for interacting hysterons," *Phys. Rev. E*, vol. 104, no. 5, p. 054608, 2021.
- [45] M. Mungan and M. M. Terzi, "The structure of state transition graphs in systems with return point memory: I. general theory," in *Ann. Henri Poincare*, vol. 20, pp. 2819–2872, Springer, 2019.
- [46] C. W. Lindeman and S. R. Nagel, "Multiple memory formation in glassy landscapes," *Sci. Adv.*, vol. 7, no. 33, p. eabg7133, 2021.
- [47] N. C. Keim and J. D. Paulsen, "Multiperiodic orbits from interacting soft spots in cyclically sheared amorphous solids," *Sci. Adv.*, vol. 7, no. 33, p. eabg7685, 2021.
- [48] J. D. Paulsen and N. C. Keim, "Minimal descriptions of cyclic memories," *Proc. R. Soc. A*, vol. 475, no. 2226, p. 20180874, 2019.
- [49] F. Preisach, "Über die magnetische nachwirkung," *Zeitschrift für physik*, vol. 94, no. 5, pp. 277–302, 1935.
- [50] M. M. Terzi and M. Mungan, "State transition graph of the preisach model and the role of return-point memory," *Phys. Rev. E*, vol. 102, no. 1, p. 012122, 2020.
- [51] T. Sagawa, "Thermodynamic and logical reversibilities revisited," *J. Stat. Mech.: Theory Exp.*, vol. 2014, no. 3, p. P03025, 2014.

BIBLIOGRAPHY

- [52] C. Merrigan, D. Shohat, C. Sirote, Y. Lahini, C. Nisoli, and Y. Shokef, "Disorder, multistability, and mechanical memory in an ordered metamaterial," *arXiv preprint arXiv:2204.04000*, 2022.
- [53] X. Guo, M. Guzman, D. Carpentier, D. Bartolo, and C. Coulais, "A little frustration to sharpen the metamaterial," *arXiv preprint arXiv:2111.13933*, 2021.
- [54] B. Pisanty, E. C. Oğuz, C. Nisoli, and Y. Shokef, "Putting a spin on metamaterials: Mechanical incompatibility as magnetic frustration," *SciPost Phys.*, vol. 10, no. 6, p. 136, 2021.
- [55] V. C. Nguyen, L. Chen, and K. Halterman, "Total transmission and total reflection by zero index metamaterials with defects," *Phys. Rev. Lett.*, vol. 105, no. 23, p. 233908, 2010.
- [56] J. Ding and M. van Hecke, "Sequential snapping and pathways in a mechanical metamaterial," *J. Chem. Phys.*, vol. 156, no. 20, p. 204902, 2022.
- [57] I. Regev, I. Attia, K. Dahmen, S. Sastry, and M. Mungan, "Topology of the energy landscape of sheared amorphous solids and the irreversibility transition," *Phys. Rev. E*, vol. 103, no. 6, p. 062614, 2021.
- [58] T. Jules, A. Reid, K. E. Daniels, M. Mungan, and F. Lechenault, "Delicate memory structure of origami switches," *Phys. Rev. Res.*, vol. 4, no. 1, p. 013128, 2022.
- [59] J. Deutsch, A. Dhar, and O. Narayan, "Return to return point memory," *Phys. Rev. Lett.*, vol. 92, no. 22, p. 227203, 2004.
- [60] J. Goicoechea and J. Ortín, "Hysteresis and return-point memory in deterministic cellular automata," *Phys. Rev. Lett.*, vol. 72, no. 14, p. 2203, 1994.
- [61] J. D. Paulsen, N. C. Keim, and S. R. Nagel, "Multiple transient memories in experiments on sheared non-brownian suspensions," *Phys. Rev. Lett.*, vol. 113, no. 6, p. 068301, 2014.
- [62] N. C. Keim, J. Hass, B. Kroger, and D. Wiekler, "Global memory from local hysteresis in an amorphous solid," *Phys. Rev. Res.*, vol. 2, no. 1, p. 012004, 2020.

- [63] M. Adhikari and S. Sastry, "Memory formation in cyclically deformed amorphous solids and sphere assemblies," *Eur. Phys. J. E: Soft Matter Biol. Phys.*, vol. 41, no. 9, pp. 1–17, 2018.
- [64] K. Matan, R. B. Williams, T. A. Witten, and S. R. Nagel, "Crumpling a thin sheet," *Phys. Rev. Lett.*, vol. 88, no. 7, p. 076101, 2002.
- [65] Y. Lahini, O. Gottesman, A. Amir, and S. M. Rubinstein, "Nonmonotonic aging and memory retention in disordered mechanical systems," *Phys. Rev. Lett.*, vol. 118, no. 8, p. 085501, 2017.
- [66] J. T. Overvelde, T. Kloek, J. J. D'haen, and K. Bertoldi, "Amplifying the response of soft actuators by harnessing snap-through instabilities," *Proc. Natl. Acad. Sci. U. S. A.*, vol. 112, no. 35, pp. 10863–10868, 2015.
- [67] M. Stern, V. Jayaram, and A. Murugan, "Shaping the topology of folding pathways in mechanical systems," *Nat. Commun.*, vol. 9, no. 1, pp. 1–8, 2018.
- [68] D. M. J. Dykstra, J. Busink, B. Ennis, and C. Coulais, "Viscoelastic snapping metamaterials," *J. Appl. Mech.*, vol. 86, no. 11, p. 111012, 2019.
- [69] S. Janbaz, K. Narooei, T. Van Manen, and A. Zadpoor, "Strain rate-dependent mechanical metamaterials," *Sci. Adv.*, vol. 6, no. 25, p. eaba0616, 2020.
- [70] G. Librandi, E. Tubaldi, and K. Bertoldi, "Programming nonreciprocity and reversibility in multistable mechanical metamaterials," *Nat. Commun.*, vol. 12, no. 1, pp. 1–9, 2021.